Research Article

International Journal of
Protective Structures

A shock tube facility to generate blast loading on structures

International Journal of Protective Structures
2016, Vol. 7(3) 340–366

DOI: 10.1177/2041419616666236
prs.sagepub.com
SAGE

Vegard Aune[1,2], Egil Fagerholt[1,2], Magnus Langseth[1,2] and Tore Børvik[1,2]

Abstract

This study evaluates the performance of a new shock tube facility used to produce blast loading in controlled laboratory environments. The facility was found to generate a planar shock wave over the tube cross section by measuring the pressure distribution on a massive steel plate located at the end of the tube. The properties of the shock wave proved to be a function of driver length and driver pressure, and the positive phase of the measured pressure–time histories was similar to those generated from actual far-field explosive detonations. However, the shock tube is also suited to investigate fluid–structure interaction effects and the behaviour of materials in blast events. This was demonstrated using a three-dimensional digital image correlation technique to measure the deformation field of thin steel plates. Synchronization of the three-dimensional digital image correlation and pressure measurements enabled a thorough investigation of the entire experiment and identification of fluid–structure interaction effects. Finally, one-dimensional numerical simulations were performed to investigate the wave patterns during the experiments.

Keywords

Experimental techniques, shock tube, far-field airblast loading, three-dimensional digital image correlation, fluid–structure interaction

Introduction

Protection of critical infrastructure against blast loading has received a lot of attention in recent years (see Børvik et al., 2009; Larcher and Casadei, 2010; Rigby et al., 2015). Blast events in such environments often involve fluid–structure interaction (FSI) in complex geometries, resulting in large deformations and potential failure and fragmentation of the structure. An essential presumption in predicting the structural response in these situations is an accurate description of the material behaviour and blast–structure interaction during the event. A large variety of analytical models

[1]Structural Impact Laboratory (SIMLab), Department of Structural Engineering, Norwegian University of Science and Technology (NTNU), Trondheim, Norway
[2]Centre for Advanced Structural Analysis (CASA), Norwegian University of Science and Technology (NTNU), Trondheim, Norway

Corresponding author:
Vegard Aune, Structural Impact Laboratory (SIMLab), Department of Structural Engineering, Norwegian University of Science and Technology (NTNU), NO-7491 Trondheim, Norway.
Email: vegard.aune@ntnu.no

are available for design and assessment of the structures exposed to blast loading, but these methods are often based on several assumptions regarding the spatial and temporal distribution of the loading. In general, they neglect blast–structure interaction effects during the response of flexible structures which may result in exaggerated conservative designs. The most appealing alternative for blast wave mitigation is increased distance between the explosive charge and the target. However, this is not always feasible in urban areas because at some point the cost of increased distance becomes questionable. Hence, there is a need for innovative and optimized solutions considering safety as well as architectural requirements.

Previous research has shown that FSI effects can mitigate the blast load acting on the structure (Hanssen et al., 2002; Langdon et al., 2010; Vaziri and Hutchinson, 2007), especially in situations involving large deformations (Kambouchev et al., 2007; Subramaniam et al., 2009). This implies that large deformations and energy absorption in structural members are favourable, since the blast wave is partially absorbed through various deformation mechanisms in the structure. The overall design can then be performed in a more economical manner without the risk of a total collapse of the entire building. Utilizing ductile materials and permitting finite deformations and inelastic strains in the design of structural members will serve as alternative load paths. However, this requires a thorough understanding of the governing physics in the problem. Depending on the blast intensity, the response of the structure may become significantly different.

Due to the complexity in both the loading and the resulting response, advanced numerical methods are required for sufficient insight. Before using such computational methods, their performance should be validated in terms of reliability, robustness and effectiveness in predicting both the loading and the response. Experimental validation is ideal since it represents the actual physics of the problem, and controlled small-scale experiments could therefore be used to validate the current computational methods and improve the understanding of the structural response during blast events. An alternative to explosive detonations is the shock tube technique (see Andreotti et al., 2015; Aune et al., 2015; Colombo et al., 2011; LeBlanc et al., 2007; Lloyd et al., 2010). This is a well-known experimental technique within the field of gas dynamics using well-defined and easily controllable initial conditions providing good repeatability of each test. The shock tube presented in this study is developed for blast applications where the properties of a planar shock wave acting on a structure may be studied by placing a test object inside or at the end of the tube. This shock tube therefore allows for the evaluation of blast–structure interaction without the need to consider the inherent complexity in close-in and near-field detonations.

The objective of this study is to investigate the performance of a new shock tube facility in generating a loading similar to that from actual free-field explosive detonations. The performance of the shock tube with respect to blast loading is evaluated with respect to requirements given in European (NS-EN 13123-1, 2001; NS-EN13124-1, 2001) and International (ISO 16934, 2007) standards. This is done by comparing the pressure–time histories in the shock tube to relevant blast load models found in the literature (Kingery and Bulmash, 1984; UFC 3-340-02, 2008). The dynamic response of deformable plates and the corresponding FSI effects are also studied experimentally using synchronized pressure measurements and two high-speed cameras in a stereovision setup, in which the deformation field was found using three-dimensional digital image correlation (3D-DIC). Finally, the numerical simulations are performed to study the wave patterns during the experiments.

Shock tube principle and operation for blast applications

Before presenting the experimental programme and findings, a brief presentation of the basic principle, operation and distinctive features of an idealized shock tube with application to blast

loading will be given. Although the fundamental aspects of these topics are well established in the literature, such a presentation is necessary for the understanding and discussion of the results later in this study.

The scope is limited to a compressed gas–driven shock tube with a closed-end configuration and constant tube cross section. It consists of a high-pressure chamber (called *driver* section) which is separated from a low-pressure chamber (denoted *driven* section) by a diaphragm. A sudden opening of the diaphragm generates a shock wave and rarefaction waves with the corresponding discontinuities. Figure 1 illustrates the events occurring in such an idealized shock tube for blast applications with a right-running shock wave and left-running rarefaction waves (i.e. $p_4 > p_1$). It is emphasized that the subindices of the pressures and velocities in the following refer to the respective regions in Figure 1.

At time $t = 0$, the diaphragm is ruptured (Figure 1(a)), generating a shock wave moving into the gas at low pressure p_1 and rarefaction waves that expand into the gas at higher pressure p_4 (Figure 1(b)). The high-pressure gas acts as a piston expanding into the low-pressure chamber and generates a shock wave moving at a velocity u_s larger than the sonic velocity a_1 of the undisturbed driven gas. The shock wave induces a mass (or particle) motion with velocity u_2 and pressure p_2 immediately behind the shock wave by compressing, heating and accelerating the driven gas in region 1. This near-instantaneous acceleration of the driven gas is accompanied by a jump in pressure, temperature and density over the shock front. The shock wave has a thickness in the order of nanometres and (in the ideal case) the compressed gas reaches its equilibrium values of pressure, density and temperature in this distance (i.e. within the timescale of nanoseconds).

The initial interface between the high-pressure and low-pressure chambers (Figure 1(a)) moves from the diaphragm at a velocity u_2 and is called the contact surface (Figure 1(b)). At the same time, as the shock wave propagates downstream the diaphragm, a system of rarefaction waves develops in the expanding high-pressure gas. This series of rarefaction waves are denoted E in Figure 1(b) and will reflect from the rear end of the driver section and then travel to the right and in the same direction as the shock wave (Figure 1(c)). If the driver section is short enough, these reflected rarefaction waves catch up with the contact surface and shock wave before reaching the test object (Figure 1(d)). The shock then decays in strength, increases in duration and decreases in velocity as it propagates towards the test specimen as a blast wave. The decreasing velocity is due to the rarefaction waves which reduce the driving pressure and hence the shock wave velocity. The experimental setup shown in Figure 1 differs from traditional shock tubes using a relatively small ratio between the lengths of the two pressure chambers, such that the reflected rarefaction waves catch up with the shock wave resulting in pressure profiles similar to that from an explosive detonation.

Upon reaching the end of the tube, the incoming blast wave reflects and travels back towards the left (Figure 1(e)). The gas particles behind the reflected wave have zero velocity, resulting in a build-up of pressure p_5 immediately behind the reflected wave which is significantly greater than that of the incoming wave. The shape of the reflected pressure–time history depends on the shape of the incoming wave and the relative strength between the (left-running) reflected shock wave and the remaining right-running flow behind the incoming shock wave (i.e. region E in Figure 1(d) and (e)). As the complexity of the system increases, numerical methods should be used to solve these types of interaction phenomena and wave patterns.

Finally, using a deformable plate as the blind flange of the tube, it is possible to study the interaction between the reflected blast wave and the corresponding structural response. This enables studies of FSI effects and blast mitigation by allowing for finite deformations of the test specimen.

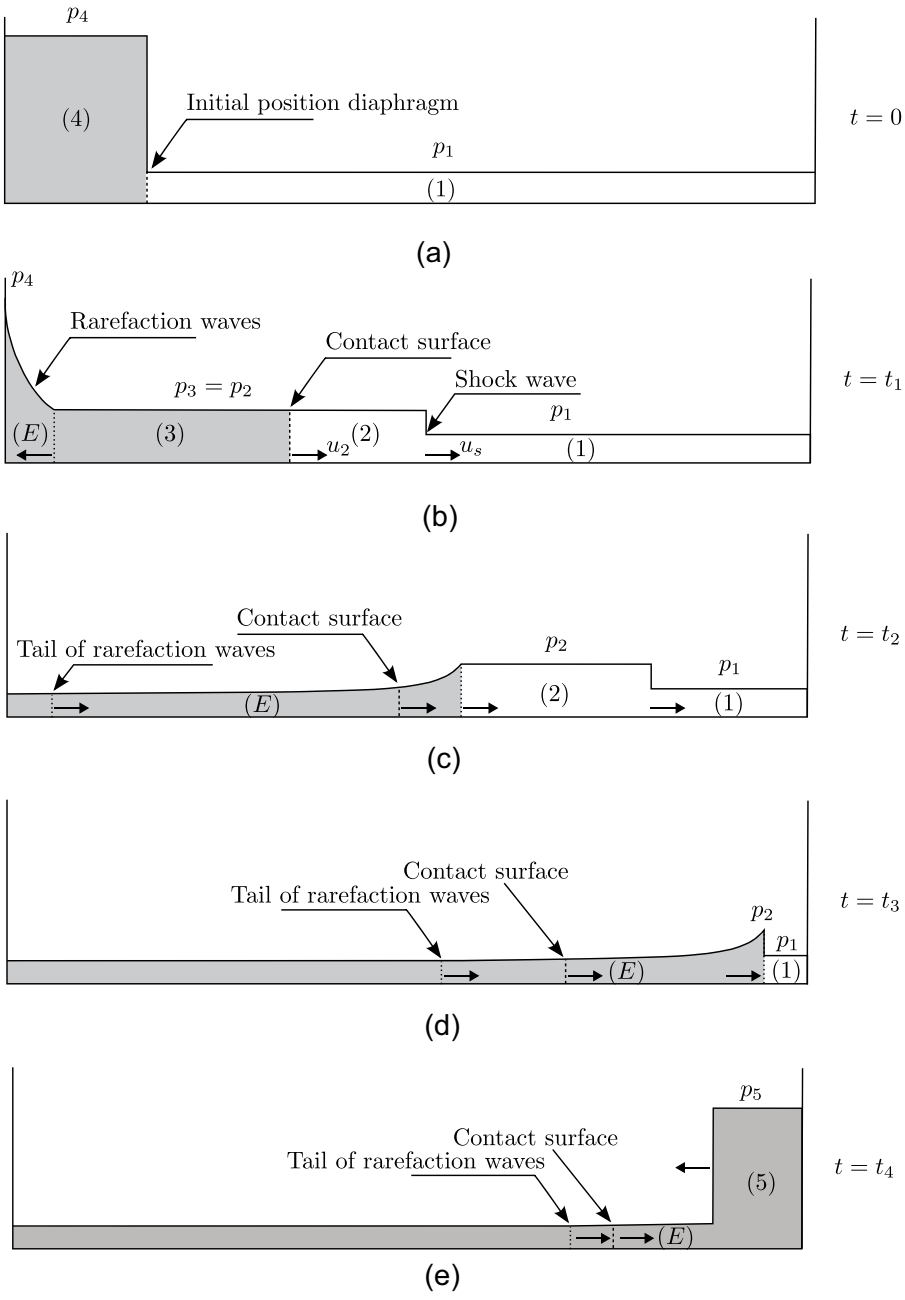

Figure 1. Schematic representation of the events occurring in a shock tube for blast applications and the corresponding pressure distributions along the longitudinal axis of the tube at characteristic times: (a) initial configuration, (b) wave pattern immediately after bursting diaphragm, (c) reflected rarefaction waves catch up with contact surface, (d) reflected rarefaction waves catch up with shock wave and (e) reflection of incoming shock wave.

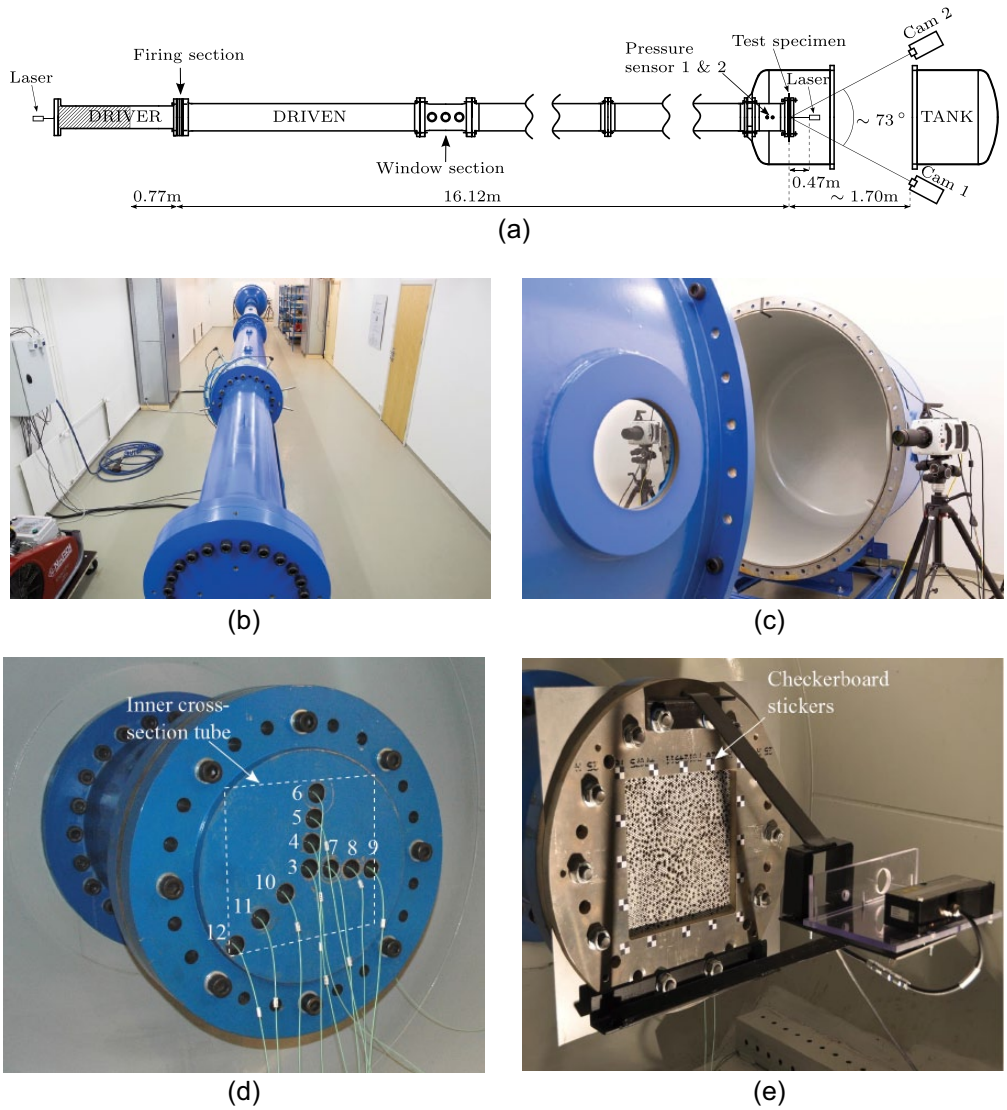

Figure 2. Experimental setup in the SIMLab Shock Tube Facility (SSTF): (a) sketch of experimental setup (seen from above), (b) the shock tube (seen from the driver), (c) high-speed cameras next to the tank, (d) picture of massive steel plate (seen from the cameras) and (e) picture of clamping, DIC speckle pattern and position laser (seen from the cameras).

Experimental setup

The SIMLab Shock Tube Facility

The experiments were performed in the SIMLab Shock Tube Facility (SSTF) (Figure 2). The tube consists of several parts joined together using bolted connections of 24 M24 socket-head screws at the end flanges of each part (Figure 2(a) and (b)). Rubber O-rings are recessed into the flange surfaces to ensure sealing at the joints. Each part is equipped with steel wheels and is carried by a

two-rail support of L-shaped angle brackets for convenient assembly and disassembly of the tube. This provides flexibility in varying the length of the driven section. If necessary, it is also possible to fully restrain the tube from axial movement by clamping the rear end of the driver section to the floor. The overall length of the tube is 18.355 m and it is made from stainless steel of grade P355NH which is developed for pressure purposes according to the European standard NS-EN 13445 (2014). Tolerances on the tube geometry and alignment follow the requirements in ISO 2768-1.

The driver section (Figure 2(a) and (b)) is manufactured with a total length of 2.02 m and has an inner diameter of 0.331 m where the internal wall is dull polished to obtain a smooth surface. Aluminium inserts may be used to vary the length of the driver section in 0.25 m increments. The driver is followed by a 0.14-m-long firing section which consists of several intermediate pressure chambers separated by diaphragms. This enables the total pressure difference between the driver and driven sections to be achieved stepwise. Several ports have been machined on the driver flange and circumference of the firing section to provide connections to pressure sensors, venting and evacuation lines. The experiment starts by filling the driver and firing sections with compressed air, where the pressures in the intermediate chambers are operated below the diaphragm rupture strength such that the desired pressure p_4 is obtained in the driver. A LabVIEW program has been developed and solenoid valves (ASCO Series 223) are installed on the gas-filling lines to control the filling process, making this operation fully automated based on the signals given by the pressure sensors (Baumer PBMN-24B31) monitoring the driver and intermediate pressure chambers. Rupture of the diaphragms is initiated by controlled and rapid venting of the intermediate pressure closest to the driver section, using two solenoid valves (ASCO Series 223). This ensures a controlled rupture of the diaphragms and reproducible bursting pressures. The bursting pressure may be varied by changing the thickness of the diaphragms. Melinex sheets are used as diaphragms due to its strength and repeatability.

The inner cross section in the driven section starts with a transition from circular to a square cross section, where an epoxy material is used to obtain a smooth surface and a square cross section of $0.3\,\text{m} \times 0.3\,\text{m}$ inside the surrounding tube. The epoxy material works as a practically incompressible material while the surrounding tube ensures the structural strength. The square cross section downstream the firing section was chosen to enable the installation of test objects in threaded holes in the tube floor and to accommodate plane parallel windows (see window section in Figure 2(a)) which simplifies the use of optical techniques (such as high-speed cameras). The driven section ends in a tank of 5.1 m^3 with an internal diameter of 1.6 m (Figure 2(a) to (c)). This enables mounting of larger test specimens (exposed to localized blast loading) at the end of the tube and an increase in volume and overall decrease in pressure after the experiment.

Piezoelectric pressure sensors (Kistler 603B), corresponding charge amplifiers (Kistler 5064) and data acquisition system from National Instruments (NI USB-6356) are used to measure the pressure downstream the firing section. The mounting of pressure sensors is possible at 20 locations along the driven section using threaded adapters (Kistler 6501) flush mounted with the internal wall of the tube. A thin layer of insulating silicone (Kistler 1051) is used to shield the pressure sensors against heat transfer from the shock wave since the sensors are only designed for temperatures up to 200°C.

The maximum working pressure of the driver section is limited to 17 MPa while the driven section, window section and tank are limited to 10, 5 and 1.4 MPa, respectively. All respective parts of the SSTF have been tested at a static pressure 45% higher than the working pressure for a few minutes to ensure sufficient strength for routine use.

Experimental programme

Aluminium inserts of diameter 0.33 m were used to reduce the volume in the driver to 23.2 and 66.3 dm^3. This is equivalent to driver lengths of 0.27 and 0.77 m, respectively, where the latter

Table 1. Experimental program.

Test	Initial conditions		
	Pressure driver (p_4) (kPa)	Pressure driven (p_1) (kPa)	Ambient temperature ($T = T_4 = T_1$) (°C)
R27-05	661.8	100.3	20.5
R27-7.5	866.4	99.8	22.6
R27-10	1200.8	100.3	20.8
R27-15	1608.5	100.3	20.9
R27-20	2127.0	100.6	21.1
R27-25	2458.8	100.3	21.4
R27-35	3330.0	100.5	21.6
R27-40	3990.1	100.5	21.8
R27-60	6024.7	99.8	22.8
R27-75	7104.8	99.9	22.9
R77-05	618.5	99.7	22.0
R77-10	1099.1	99.6	21.5
R77-15	1594.0	99.8	24.0
R77-20	2074.3	99.8	23.8
R77-25	2821.6	99.7	23.9
R77-35	3811.8	99.8	23.6
R77-60	6073.2	99.8	23.9
R77-75	7765.5	99.6	23.2
D77-15	1590.4	100.4	19.9
D77-35	3717.2	100.4	20.8
D77-60	6195.0	100.4	20.6

configuration is illustrated in Figure 2(a). The loading was varied by changing the initial pressure p_4 in the driver section, while the initial pressure in the driven section was operated at ambient conditions. Table 1 gives the complete test matrix, where each test is numbered XY-Z in which X denotes rigid (R) or deformable (D) test specimens, Y is the driver length in centimetres and Z indicates the firing overpressure (in bars) in the driver. A massive steel plate was used to obtain a rigid blind flange (Figure 2(d)), while a thin deformable plate was used to introduce moving boundary conditions (Figure 2(e)). The deformable plates were manufactured from medium-strength steel sheets of type Docol 600 DL produced by Swedish Steel Ltd (SSAB). Both the massive steel plate with thickness of 0.05 m and the deformable plate specimens with dimensions of $0.625\,\text{m} \times 0.625\,\text{m} \times 0.0008\,\text{m}$ were clamped to the end flange of the tube (Figure 2(d) and (e)) in an attempt to achieve fixed boundary conditions. The plates had an exposed area of $0.3\,\text{m} \times 0.3\,\text{m}$ (equal to the internal cross section of the tube). Material data for Docol 600 DL plates may be found in Aune et al. (2016).

A closed-end configuration of the SSTF is favourable to avoid leakage of the pressure in the circumferential direction of the test specimens at the blast–structure interface and will therefore maintain a uniform and plane shock wave also around the perimeter of the tube. Placing the test specimen even the smallest distance from the end of the tube would lead to a non-uniform spatial and temporal distribution around the periphery of the tube, due to partial venting of the gas into the expanding tank volume (see Chennamsetty et al., 2015; Louar et al., 2015). Moreover, such a venting results in rarefaction waves travelling back upstream the tube causing increased complexity of the subsequent wave patterns.

Two sensors measured the pressure behind the incident and reflected shock wave 24.5 cm (Sensor 2) and 34.5 cm (Sensor 1) upstream the test specimens (see Figure 2(a)). The pressure sensors were automatically triggered when the shock wave arrived at Sensor 1 and operated with a sampling frequency of 500 kHz. The delay in arrival time at the pressure sensors was used to determine the shock velocity u_s and the corresponding Mach number M_s. This is valuable information in validating the pressure measurements during the experiments against idealized shock tube theory (Gaydon and Hurle, 1963). Moreover, the massive plate was equipped with pressure sensors along the vertical, horizontal and diagonal to investigate the planarity of the shock wave (Figure 2(d)).

Due to large momentum changes induced in the gas during firing, considerable forces exist along the axis of the tube during the experiments. This axial recoil was accounted for by allowing the entire facility to move as a rigid body along the two-rail support. This movement was used to evaluate the accuracy of the 3D-DIC technique by comparing it to the laser measurements at the rear end of the driver section (see Figure 2(a)).

DIC measurements

A 3D-DIC technique was used to capture displacement and strain fields of the deformable plates as well as the axial movement of the entire facility during testing. Two Phantom v1610 high-speed cameras with 100-mm Nikon lenses were placed approximately 1.70 m from the plates in a symmetric stereovision setup, and the angle between the optical axes of the cameras was approximately 73° (Figure 2(a)). The recording rate was chosen to be 24 kHz in all tests with an exposure time of 30 μs and an image size of 768×800 pixels at 12-bit grey level digitization.

The camera models, that is, the mathematical relation between 3D target coordinates and image coordinates, were calibrated by recording a set of image pairs of calibration targets with known geometries. These images were used to extract a set of corresponding image and target coordinates which served as the input for the camera model optimization. The calibration targets were located at the end of the tube (Figure 3), where two different calibration targets were applied to find the most suitable calibration procedure for this particular setup, that is, a cylinder with 80-mm diameter and a 10-mm-thick glass plate. A total of 16 image pairs of the glass-plate target and 8 image pairs of the cylinder target were recorded. The calibration targets were translated and rotated between each recording. Checkerboard patterns with squares of 6.527 and 4.669 mm were printed on the surface of the cylinder and glass plate, respectively. The corners of the checkerboard pattern were found for each image using a corner detection algorithm (Harris and Stevens, 1988), and 14 camera model parameters (including radial and decentring distortion) were optimized for each camera following a calibration procedure based on the work by Heikkilä (1997). The optimization procedure incorporates a non-linear least-squares algorithm to minimize the difference between the extracted image coordinates (corners) and the corresponding image coordinates calculated from known 3D target coordinates.

From the 16 glass-plate images, approximately 14,000 calibration points were extracted and used in the least-squares optimization for both cameras. The calibration points covered a volume of approximately $350\,\text{mm} \times 350\,\text{mm} \times 80\,\text{mm}$. The standard deviation of the camera model residuals in the XY-plane was 0.050 pixels (0.025 mm) for Camera 1 and 0.055 pixels (0.03 mm) for Camera 2. To evaluate the stereovision model (i.e. the coupling of the two camera models), a 3D model of the glass plate was calculated for each image pair using the extracted corners and the optimized camera models. The deviations of this 3D model compared to an exact plane were then calculated for each extracted corner. For all 16 image pairs, the standard deviation of the calculated errors was less than 0.05 mm. These minor residual errors seem to be a combination of systematic errors and random noise. It is not clear whether the systematic part of these resultant errors arises

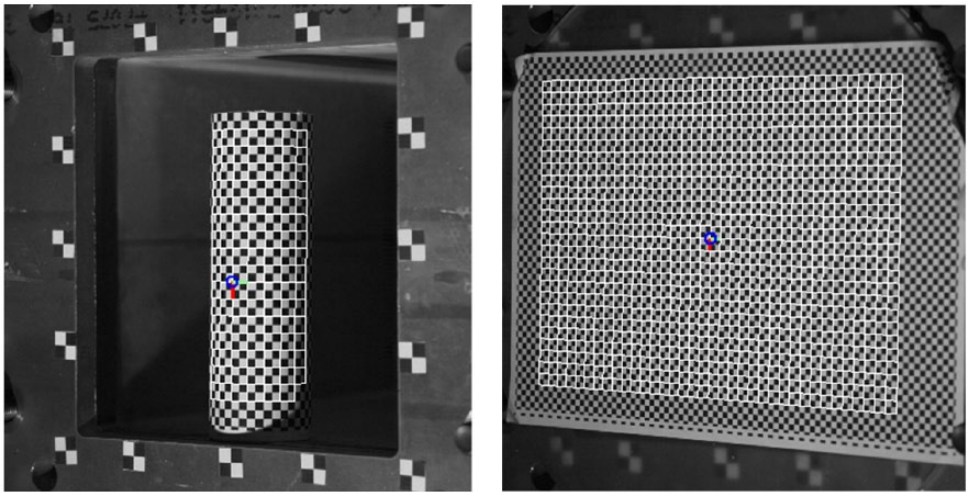

Figure 3. Calibration targets. Both images show meshes where the nodes represent extracted corners (with known target coordinates) that are used for camera calibration: (a) cylindrical calibration target and (b) glass-plate calibration target.

from inaccuracies in the calibration target or lens distortions. However, for these particular tests, these levels of errors are regarded as acceptable.

From the eight cylinder images, approximately 6000 calibration points were extracted for each camera and used for optimization. Here, the covered volume was approximately 250mm × 250mm × 60mm. The standard deviation of the camera model residuals in the XY-plane was 0.11 pixels (0.06 mm) for both cameras. Similarly, as for the glass plate, the resulting stereovision model (from the cylinder target) was checked against an exact plane. The standard deviation of the errors in the calculated 3D model (compared to an exact plane) was found to be 0.07 mm.

This implies that the glass-plate target provided slightly better calibration residuals compared to the cylinder target. This is probably because it is somewhat more challenging to create a cylinder with a checkerboard pattern with the same accuracy as a planar target. Moreover, the checkerboard pattern extraction from a curved surface may not be ideal. However, the cylinder target provides some additional features compared to a plane target. The non-coplanar calibration points from a cylinder allow a full camera model to be optimized from a single image, whereas the coplanar calibration points from a single glass-plate image cause singularities in the solution that needs special attention (Sturm and Maybank, 1999). A single-image camera model may still be beneficial from a practical point of view and serves as a robust starting point for the multiple-image least-square optimization of the camera models. Furthermore, for cylindrical targets, the relation between cylinder diameter and checkerboard square size may be exploited. Assuming that the cylinder diameter is known, the square size of the checkerboard pattern (as well as misalignment) may be optimized from the recorded images. This can provide better estimates of the checkerboard square size than those obtained with manual methods. Despite the practical advantages of using a cylinder target, the camera models optimized from the glass-plate target were used in this study since these resulted in slightly lower residuals.

Prior to each test, the deformable plates were spray-painted white before a template was used to apply a black speckle pattern with a size distribution in the range of 2–4 mm equivalent to

3.4–6.7 pixels (Figure 2(e)). The choice of speckle size was based on minimizing the effect of aliasing in the DIC (Sutton et al., 2009), and the pixel-to-millimetre ratio is estimated to be approximately 1.7 in the XY-plane for both cameras. This resulted in an effective sensor size of $21.5\,\text{mm} \times 22.4\,\text{mm}$ since the cameras operate with a pixel size of $28\,\mu\text{m} \times 28\,\mu\text{m}$ (and image size of 768×800 pixels). Image sequences from the two cameras were then post-processed using an in-house 3D-DIC code (Fagerholt, 2012) based on the finite element (FE) formulation of DIC presented by Besnard et al. (2006). Element-wise grey value normalization (both offset and scale) was applied in the DIC analyses to account for highlights observed on the surface of the test specimens (Sutton et al., 2009). These highlights were mainly caused by direct reflections of the halogen studio lights that were used during the tests. In cases where large jumps in displacements between two subsequent images were observed, a coarse-search multi-scale approach (Hild et al., 2002) was applied prior to the FE-DIC optimization of the particular image.

The axial movement of the entire facility was measured using a set of 2×2 checkerboard stickers glued to the clamping frame at the end flange (see Figures 2(e) and 3(a)). These checkerboard stickers were observed by the two cameras during the test. The centre corner of the checkerboard patterns was also tracked using the corner finder algorithm (Harris and Stevens, 1988) and subsequently coupled with the camera models to provide the movement in 3D space.

Experimental validation

Shock tube performance

The purpose of the SSTF is to produce a loading similar to that from blast events within controlled laboratory environments. Shock tubes are widely used to study structures exposed to blast loading (see Andreotti et al., 2015; Colombo et al., 2011; LeBlanc et al., 2007; Subramaniam et al., 2009); however, such studies often report the pressure–time histories without fully addressing the requirements to blast performance. According to relevant European (NS-EN 13123-1, 2001; NS-EN13124-1, 2001) and International (ISO 16934, 2007) standards, a shock tube used in blast applications should ensure the consistent reproduction of a plane shock wave normal to the surface of the test object. Moreover, the positive phase of the pressure–time history should be of a form which can be related to that from a spherical unconfined high explosive charge of a known weight of trinitrotoluene (TNT) detonating at a known distance from the target. The blast performance may be assessed using a massive steel plate equipped with pressure sensors distributed over the cross-sectional area of the tube. This enables an investigation of the planarity of the shock wave, and the pressure–time histories may be related to approximate free-field airblast conditions resulting in similar blast loads as experiments with spherical and hemispherical explosive detonations found in the literature (Kingery and Bulmash, 1984; UFC 3-340-02, 2008). This approach was used by Lloyd et al. (2010) and Riedel et al. (2010) and will also be used in the following to evaluate the blast performance of the SSTF with the closed-end configuration presented in section ‘Experimental programme’.

The spatial and temporal pressure distribution was therefore evaluated by comparing the time of arrival t_a and pressure magnitudes at the sensors along the vertical, horizontal and diagonal of the massive plate (Figure 2(d)). Figure 4 contains the results from two representative tests, where Sensor 3 was located at the centre, Sensors 4–6 along the vertical, Sensors 7–9 along the horizontal and Sensors 10–12 along the diagonal. The number of sensors was limited by the available channels in the data acquisition system, and all sensors were flush mounted with the internal surface of the massive steel plate. Also note that Sensors 6 and 9 were positioned 15 mm from the inner walls, while Sensor 12 was positioned in the very corner of the cross section (Figure 2(d)). It was found that the SSTF produced a near-planar shock wave with a maximum variation of 0.002 ms arrival

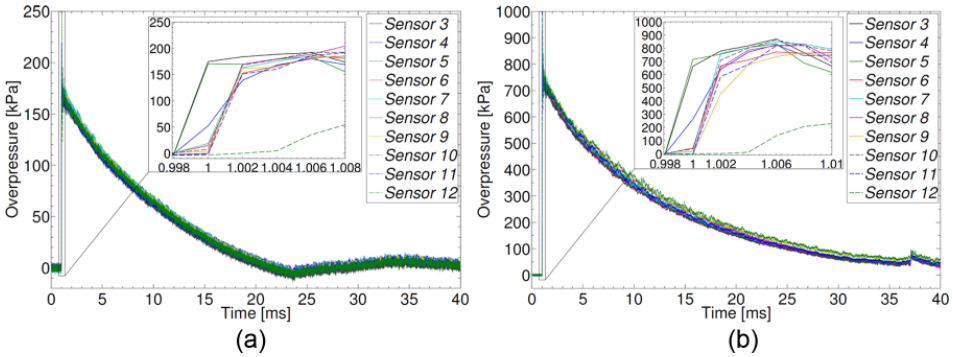

Figure 4. Pressure measurements at the centre (Sensor 3), along the vertical (Sensors 4–6), horizontal (Sensors 7–9) and diagonal (Sensors 10–12) of the massive steel plate for two representative tests: (a) R27-05 and (b) R27-40.

time. This was similar to the sampling rate (500 kHz) and the shock wave can therefore be considered as planar. The only exception was the measurements from Sensor 12 (see Figure 4), which was located in the corner of the cross section and therefore experienced some minor corner effects. This is expected when operating with square cross sections because the velocity is approaching 0 near the walls due to friction effects. However, negligible influence of these friction effects in the sensors closest to the walls (Sensors 6 and 9) was seen. Therefore, only the pressure measurement at the centre of the plate (i.e. Sensor 3) is used in the following to represent the pressure at the massive steel plate.

Figure 4 also shows that the loading is characterized by the same distinctive features as the positive phase of a blast wave from a high explosive detonation. That is, an almost instantaneous rise (within the timescale of microseconds) from atmospheric pressure p_1 to a peak reflected (head-on) overpressure $p_{\mathrm{r,max}}$, followed by an exponential decay in pressure back to the ambient pressure over a period in time known as the positive phase duration t_{d+} (typically in milliseconds). It is emphasized that the wave fronts and interaction of waves will continue back and forth in the tube until a static overpressure is reached when the gas comes to rest (see section 'Shock tube principle and operation for blast applications' and Figure 1). This is seen as multiple peaks (secondary and tertiary reflections) of decreasing magnitude on the pressure measurements and leads to multiple loading events on the plate such that the final configuration may not be representative for the primary loading event. However, the relevant timescale of the experiments depends on the application and therefore limits the time-window of interest. The time-window of interest in these experiments is limited to the first positive part of the overpressure history. Note that tertiary reflections are the internal reflections within the tube as the reflected wave interacts with the end of the driver section and returns to the massive plate. The timing of these reflections depends on the driver pressure p_4 and the ratio between the lengths of the driver and driven sections. Using a sufficiently long driven section, these reflections occur after the end of the first positive phase.

Figure 5 and Table 2 present the measured blast properties (reflected overpressure, duration, impulse and Mach number) of the positive phase for all the driver pressures and driver lengths in Table 1. It is evident that the blast properties are a function of both the driver length and driver pressure, where (as expected) larger driver pressures result in increasing magnitudes of the blast properties. It is also seen that the driver length has a significant influence on the blast properties, where the reflected overpressure $p_{\mathrm{r,max}}$ for the largest length (0.77 m) was almost twice that

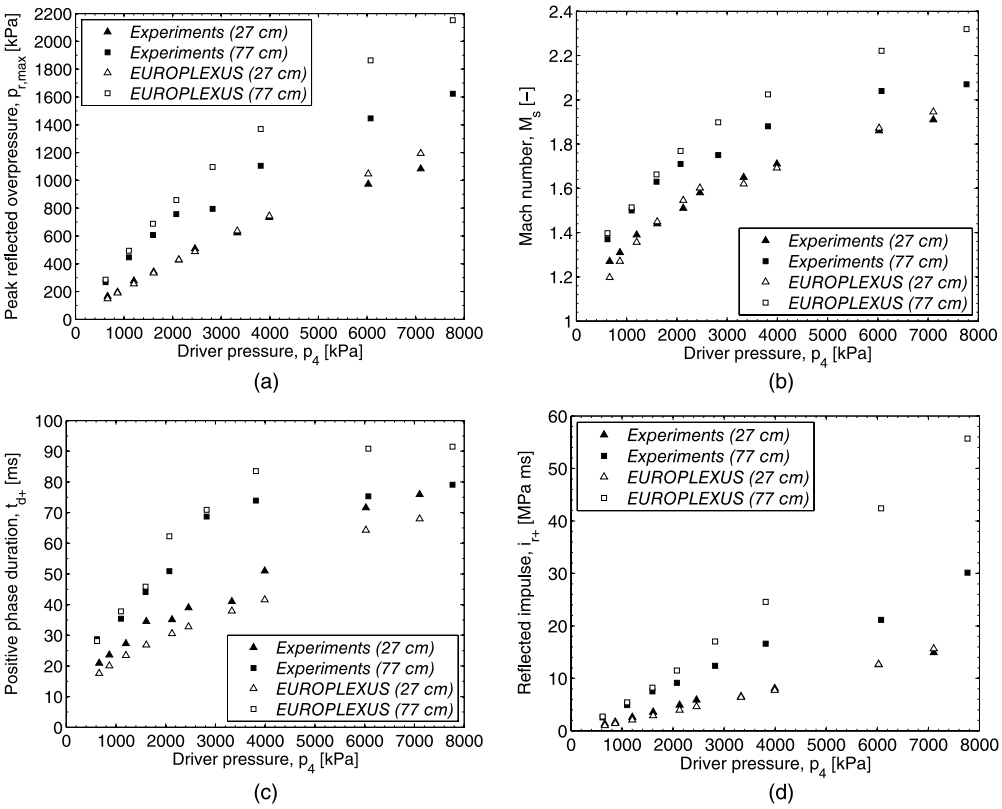

Figure 5. Blast parameters as a function of driver length and driver pressure. The time-window of interest is limited to the positive phase measured by Sensor 3: (a) peak reflected overpressure $p_{r,max}$, (b) Mach number M_s, (c) positive phase duration t_{d+} and (d) reflected impulse i_{r+}.

produced from the smallest length (0.27 m) for approximately the same bursting pressures (see Figure 5(a) and Table 2). Following the argumentation in section 'Shock tube principle and operation for blast applications', this is explained by the fact that larger driver pressures p_4 result in larger Mach numbers M_s (Figure 5(b)) and increasing driver lengths delay the reflected rarefaction waves in catching up with and slowing down the shock wave. The shock wave velocity was determined based on the pressure measurements at Sensors 1 and 2 (Figure 2(a)) and by dividing the distance between their respective locations (0.1 m) by the delay in time of arrival. It should be noted that Sensor 6 (see Figure 2(d)) and Sensor 2 could provide an even better estimate of the shock velocity; however, it was chosen to focus on the performance of Sensors 1 and 2 because these will be used in future investigations involving deformable plates. In general, the shock wave was characterized by supersonic velocities $(M_s > 1)$ since the rate of propagation exceeds the speed of sound a_1 in the driven section (Figure 5(b)). Moreover, increasing driver pressures and driver lengths produce shock waves with a longer positive phase duration t_{d+} (Figure 5(c)). A noticeable effect of the driver length on the positive phase duration is observed due to the increased volume of compressed air released at the respective bursting pressures. The combination of increasing peak reflected overpressures (Figure 5(a)) and positive phase durations (Figure 5(c)) results in an increase in the corresponding impulse i_{r+} (Figure 5(d)), where the impulse i_{r+} was found by numerical integration of the reflected overpressure during the positive phase duration. Note that

Table 2. Measured blast parameters at Sensors 1–3 and Friedlander parameters curve-fitted to data from Sensor 3.

Test	Parameters (Sensors 1 and 2)		Friedlander parameters (Sensor 3)				Shock tube theory		Deviation experiment versus theory	
	M_s (−)	$p_{so,max}$ (kPa)	$p_{r,max}$ (kPa)	t_{d+} (ms)	b (−)	i_{r+} (kPa ms)	$p_{so,max}$ (kPa)	$p_{r,max}$ (kPa)	$\Delta p_{so,max}$ (%)	$\Delta p_{r,max}$ (%)
R27-05	1.27	71.7	166.3	20.9	0.900	1316.8	71.7	183.3	0.0	−10.2
R27-7.5	1.31	82.3	196.3	23.6	1.011	1675.6	83.4	220.1	−1.3	−12.1
R27-10	1.39	111.4	276.7	27.3	1.237	2587.2	109.1	306.1	2.1	−10.6
R27-15	1.44	133.2	341.6	34.5	1.692	3576.8	125.6	365.7	5.7	−7.0
R27-20	1.51	164.3	427.6	35.1	1.390	4906.1	150.2	459.0	8.6	−7.3
R27-25	1.58	189.2	508.7	39.0	1.664	5883.9	175.1	559.9	7.5	−10.1
R27-35	1.65	223.1	622.7	41.0	2.072	6544.3	202.0	674.2	9.5	−8.3
R27-40	1.71	253.9	732.8	51.0	1.847	8081.1	225.6	779.9	11.1	−6.4
R27-60	1.86	326.1	973.1	71.6	2.721	12,608.4	286.4	1072.3	12.2	−10.2
R27-75	1.91	352.6	1083.2	75.9	2.417	14,907.6	308.6	1184.3	12.5	−9.3
R77-05	1.37	108.0	267.5	28.7	1.306	2557.9	102.0	282.0	5.6	−5.4
R77-10	1.50	161.7	446.2	35.4	1.571	4904.5	145.3	440.8	10.2	1.2
R77-15	1.63	219.1	606.6	44.1	2.025	7510.0	192.9	636.3	11.9	−4.9
R77-20	1.71	260.8	756.8	50.9	2.666	9147.0	224.0	774.4	14.1	−2.3
R77-25	1.75	274.7	795.2	68.7	2.044	12,383.3	239.9	848.0	12.7	−6.6
R77-35	1.88	365.9	1105.2	73.9	1.904	16,613.4	295.1	1116.0	19.4	−1.0
R77-60	2.04	429.4	1446.1	75.3	1.768	21,151.7	368.1	1498.4	14.3	−3.6
R77-75	2.07	460.2	1623.2	79.1	1.088	30,149.0	381.7	1573.7	17.1	3.1

Peak incident and reflected overpressures compared to the idealized shock tube theory using equations (3) and (4).

before determining the properties of the blast loading in Figure 5 and Table 2, the experimental data were low-pass filtered with a cutoff frequency of 0.15 times the sampling rate (500 kHz). This enabled consistent determination of the blast parameters and reduced the effect of high-frequency oscillations in the pressure measurements without altering the characteristic shape of the curves. Such high-frequency oscillations (see Figure 4) are due to the relatively high eigen frequency of the pressure sensors and the high sampling rate used to capture the near-instantaneous rise in pressure over the shock front.

The modified Friedlander equation (Friedlander, 1946) is typically used to represent the pressure–time history when the parameters governing the positive phase are known, that is

$$p_r(t) = p_1 + p_{\mathrm{r,max}}\left(1-\frac{t-t_a}{t_{d+}}\right)\exp\left(\frac{-b(t-t_a)}{t_{d+}}\right), \quad t_a < t < t_a + t_{d+} \tag{1}$$

where the positive impulse has an analytical solution given by

$$i_{r+} = \int_{t_a}^{t_a+t_{d+}} p_r(t)dt = \frac{p_{\mathrm{r,max}}t_{d+}}{b^2}\left[b-1+\exp(-b)\right] \tag{2}$$

The blast parameters in Table 2 (i.e. $p_{\mathrm{r,max}}$, t_{d+} and i_{r+}) were used to iteratively find the exponential decay coefficient b in equation (2), which enables the corresponding Friedlander curve to be expressed by equation (1). A selection of representative Friedlander curves is compared to the corresponding experiments in Figure 6, while the Friedlander parameters for all tests are given in Table 2. Note that the experimental data from Sensors 1 and 2 are also included in Figure 6, and that time 0 ($t = 0$) is taken as the arrival of the shock wave at Sensor 1 located upstream the test specimen (Figure 2(a)). Figure 6 shows excellent agreement between the Friedlander curves and experimental data until secondary reflections occur during the positive phase duration (Figure 6(e) and (f)). These secondary reflections occurred at larger driver pressures and driver lengths, that is, in test R27-60, R27-75 and R77-25 to R77-75. In the particular cases of secondary reflections, the exponential decay parameter b was determined by using the peak reflected overpressure $p_{\mathrm{r,max}}$, positive phase duration t_{d+} and curve-fitting of equation (1) to the experimental curves until the secondary reflections occurred. Thus, equation (2) was not used in the case of secondary reflections.

A well-established reference for the properties of the positive phase from airblast experiments is the research by Kingery and Bulmash (1984). They used spherical and hemispherical charges of TNT detonating at a given stand-off distance R from an infinite reflecting surface and curve-fitted a large set of experimental data to high-order polynomials. These empirical relations are widely used in the literature (see UFC 3-340-02, 2008). The peak reflected overpressure $p_{\mathrm{r,max}}$, corresponding impulse i_{r+} and the empirical relations by Kingery and Bulmash were therefore used to relate the pressure histories in the shock tube to approximate free-field conditions (i.e. a particular weight W of TNT detonating at a given distance R from the target). The approximate free-field conditions are given in Table 3 for selected tests, while Figure 7 compares the corresponding pressure histories to tests R27-05 and R27-20. It is seen that the shock waves generated in the SSTF closely resemble that from high explosive far-field detonations (Table 3) and that the Friedlander curves from the experiments are in good agreement with the pressure histories from the corresponding free-field conditions. Moreover, a retrospective of events (Little, 2007) and practical implications of size and weight of explosives that can be transported by personnel and various vehicles (FEMA 452, 2005) show that the SSTF is capable of generating a loading similar to that

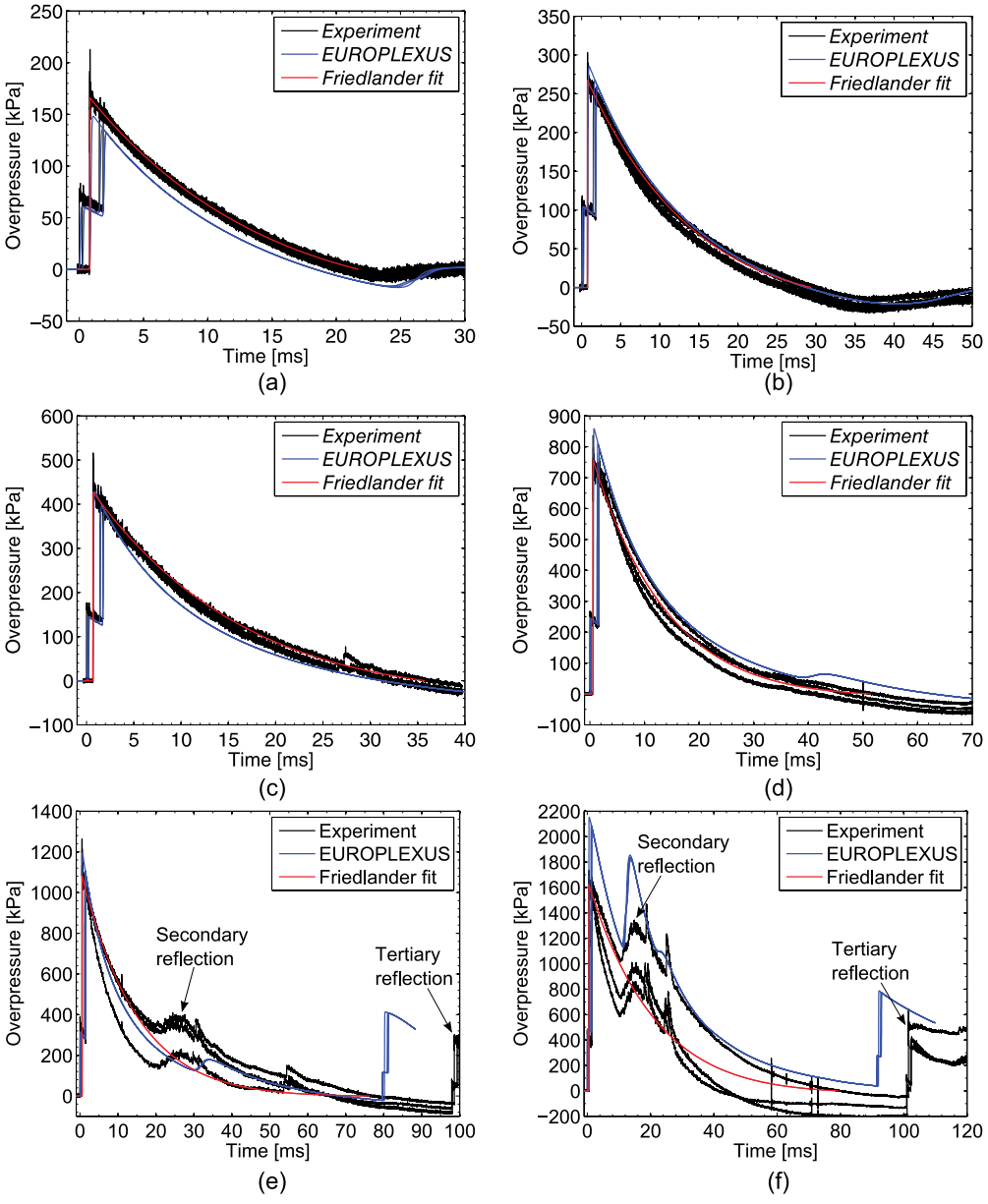

Figure 6. Representative pressure–time histories from experiments (Sensors 1–3) and corresponding numerical simulations in EUROPLEXUS. Friedlander curves fitted to Sensor 3 are also included: (a) R27-05, (b) R77-05, (c) R27-20, (d) R77-20, (e) R27-75 and (f) R77-75.

of representative free-field detonations at typical stand-off distances used in protective design (NS-EN 13123-1, 2001; NS-EN13124-1, 2001).

Finally, knowing the shock velocity and Mach number $M_s = u_s / a_1$ from the experiment (see Table 2), the idealized shock theory may be used to calculate the peak incident (side-on) overpres-

Table 3. Experimental results on the massive plate and corresponding charges of TNT at given stand-off distances.

Test	Friedlander parameters		Spherical charge			Hemispherical charge		
	$p_{r,max}$ (kPa)	i_{r+} (kPa ms)	W (kg)	R (m)	Z (m/kg$^{1/3}$)	W (kg)	R (m)	Z (m/kg$^{1/3}$)
R27-05	166.3	1316.8	1006.1	33.4	3.34	513.6	31.7	3.96
R27-7.5	196.3	1675.6	1680.6	37.0	3.11	850.5	34.9	3.69
R27-10	276.7	2587.2	3893.2	42.8	2.72	1945.9	40.1	3.21
R27-15	341.6	3576.8	7809.0	49.9	2.51	3886.5	46.6	2.96
R27-20	427.6	4906.1	15,117.4	57.2	2.31	7506.7	53.4	2.73
R27-25	508.7	5883.9	20,943.8	60.0	2.17	10,395.5	56.0	2.57
R77-05	267.5	2557.9	3932.9	43.5	2.76	1967.5	40.8	3.25
R77-10	446.2	4904.5	14,308.1	55.3	2.28	7103.5	51.7	2.69

Scaled distances ($Z = R / W^{1/3}$) are found using Hopkinson–Cranz scaling (Baker et al., 1991).

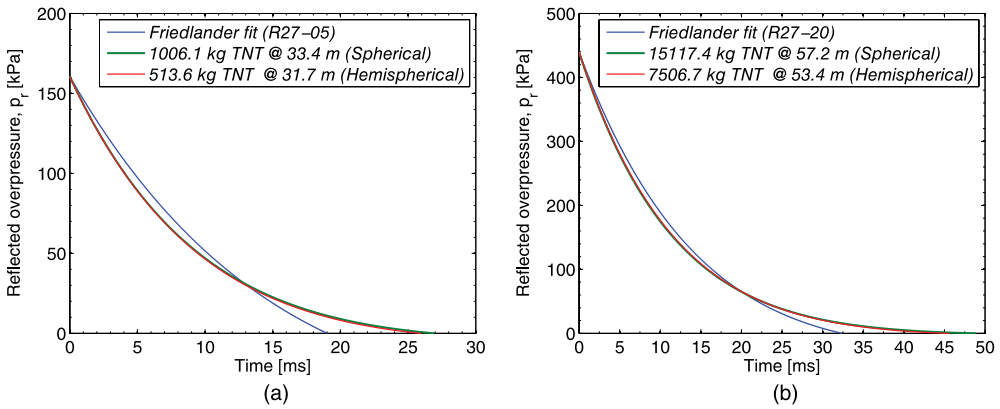

Figure 7. Experimental pressure–time histories (Friedlander fit) compared with that from approximate free-field spherical and hemispherical detonations found using the empirical equations by Kingery and Bulmash (1984): (a) R27-05 and (b) R27-20.

sure $p_{so,max}$ and the peak reflected (head-on) overpressure $p_{r,max}$, respectively, as (see, for example, Gaydon and Hurle, 1963)

$$p_{so,max} = p_2 - p_1 = p_1\left(\frac{2\gamma(M_s^2 - 1)}{\gamma + 1}\right) \tag{3}$$

and

$$p_{r,max} = p_5 - p_1 = p_{so,max}\left(\frac{\left(2 \cdot \frac{(\gamma - 1)}{\gamma + 1} + 1\right) + \frac{p_1}{p_2}}{\frac{\gamma - 1}{\gamma + 1} + \frac{p_1}{p_2}}\right) \tag{4}$$

where $\gamma = C_p / C_v$ is the ratio of specific heats given by the specific heat at constant pressure C_p and the specific heat at constant volume C_v. This representation of the shock strength is convenient since the shock velocity u_s is easily measured in the experiments. In fact, the accuracy of equation (3) is so high that this approach is often used to calibrate electronic gauges and pressure sensors (see Downes et al., 2014). Using the measured shock velocity u_s and the corresponding Mach number M_s, the rise in pressure across the shock can be determined by equation (3).

The pressures found from this idealized theory are included and compared to the experimental measurements in Table 2, where negative values of $\Delta p_{\mathrm{so,max}}$ and $\Delta p_{\mathrm{r,max}}$ imply that the theoretical values are larger than the corresponding experimental measurements. The increasing deviation of the peak incident overpressures $\Delta p_{\mathrm{so,max}}$ at larger pressures is related to the filtering of high-frequency noise of the pressure measurements, where the experimental values reported in Table 2 may still contain some noise. Moreover, the peak reflected overpressures $p_{\mathrm{r,max}}$ calculated from the idealized shock theory are conservative since the Mach number M_s is calculated based on the measurements in Sensors 1 and 2 located upstream Sensor 3. The shock velocity will continue to decrease travelling from Sensor 2 to Sensor 3 and the actual Mach number M_s immediately before the impact is slightly less than that used to calculate the reflected pressures. Nevertheless, it is seen that the experimental measurements and the idealized theory are in acceptable agreement indicating that the pressure measurements reported in this study are reliable. It should also be noted that an alternative approach to validate the pressure measurements against the idealized theory is to produce a temporally uniform pressure pulse as a basis for comparison. However, this is outside the scope of this study and suggested as future work.

Evaluation of the 3D-DIC technique

Before using the 3D-DIC technique to obtain displacement fields and to study FSI effects, it should be evaluated to ensure that the generated displacement field is reliable. A laser displacement sensor (optoNCDT 2310-50) mounted at the end of the tube was used to measure the mid-point deflection of the deformable plates (relative to the tube) during the experiments (Figure 2(e)). This was then used as the basis for comparison to ensure that the corresponding displacement predicted by 3D-DIC is reasonable. Since the high-speed cameras were located on the floor and not in contact with the SSTF (Figure 2(c)), it is necessary to correct the 3D-DIC measurements for the rigid body movement of the tube during each experiment. The 3D-DIC technique is therefore evaluated in two steps. First, the rigid body movement of the entire facility is measured by a laser positioned on the floor at the rear end of the driver (Figure 2(a)) and compared to the movement of the opposite end of the tube measured by 3D-DIC using the checkerboard stickers on the clamping frame (Figure 2(e)). Then, the mid-point deflection of the plates measured by 3D-DIC was corrected for the rigid body motion of the tube and compared to the corresponding deflection measured by the laser device (Figure 2(e)).

Typical results are shown for test D77-35 in Figure 8, where Figure 8(a) compares the rigid body movement of the entire facility and Figure 8(b) shows the measured mid-point deflection of the plate. Both the rigid body movement and the mid-point deflection measured by the laser and the 3D-DIC were in excellent agreement, and the 3D-DIC technique is therefore considered to provide accurate displacements. Note that the minor deviations in Figure 8(a) are related to the eigen oscillations in the longitudinal axis of the tube interacting with the wave pattern inside the tube, while the high-frequency noise in the laser measurements in Figure 8(b) is due to the eigen oscillations of the laser mounting frame (Figure 2(e)) induced by the recoil when the diaphragms burst. These latter oscillations are not observed in the 3D-DIC measurements since the high-speed cameras were not in contact with the tube.

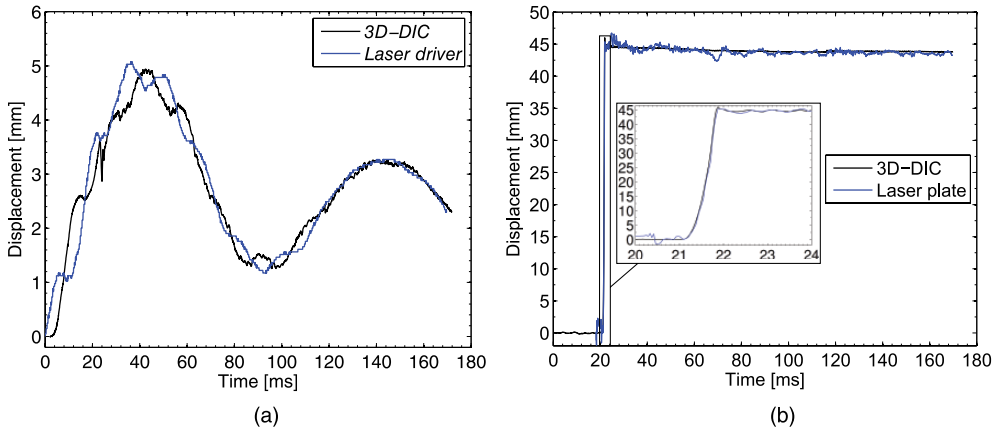

Figure 8. Evaluation of the 3D-DIC technique in predicting (a) the rigid body movement and (b) the mid-point deflection in test D77-35.

Deformable plates

Section 'Shock tube performance' proved that the SSTF is capable of producing pressure–time histories from typical threats based on a given weight and stand-off distance of high explosives. However, the SSTF is also suitable for experimental validation of computational methods used in blast-resistant design. Synchronizing the 3D-DIC measurements with the pressure recordings enables a thorough investigation of the dynamic response and FSI effects in controlled blast environments.

Figure 9 shows pressure measurements from Sensor 2 synchronized with the mid-point deflection during the 0.8-mm-thick steel plate tests (see Table 1). A dynamic elastoplastic response is observed where the permanent mid-point deflection increases with increasing reflected overpressures (Figure 9(a) to (c)). Moreover, the secondary reflection at approximately 15–25 ms (Figure 9(b) and (c)) seems to have negligible effect on the mid-point deflection. Note that the pressure is measured upstream the test specimens (Figure 2(a)) since it is challenging to mount pressure sensors in the thin plates without altering their structural characteristics. In an attempt to estimate the actual loading on the plate, equation (1) was curve-fitted to the measurements at Sensor 2 and extrapolated back to the time of impact. This approach assumes a rigid plate and can be used to discuss FSI effects.

A basic understanding of the role of FSI when the shock wave interacts with a moving boundary is given in the works of Courant and Friedrichs (1976), Toro (2009) and Subramaniam et al. (2009). That is, if the boundary (i.e. the deformable plate) starts to move, the motion alters the pressure at its surface. FSI effects could also be investigated by comparing pressure histories at Sensor 2 in the massive and deformable plate experiments with the same driver length and similar firing pressures (see R77-15, R77-35, R77-60, D77-15, D77-35 and D77-60 in Table 1). This is presented in Figure 10, while the peak reflected overpressures measured at Sensor 2 are reported in Table 4 and compared to the corresponding measurement in the massive steel plate experiments. A reduction in the reflected overpressure is observed in the tests with the deformable plates, where the reduction is more evident at increasing pressure magnitudes. It is important to emphasize that Sensor 2 is located upstream the test specimen (see Figure 2(a)), and that the peak pressure immediately after reflection is independent of the stiffness of the structure (see, for example, Subramaniam et al., 2009). Figure 10 also shows that the incident (side-on) pressures were in excellent agreement, indicating that the

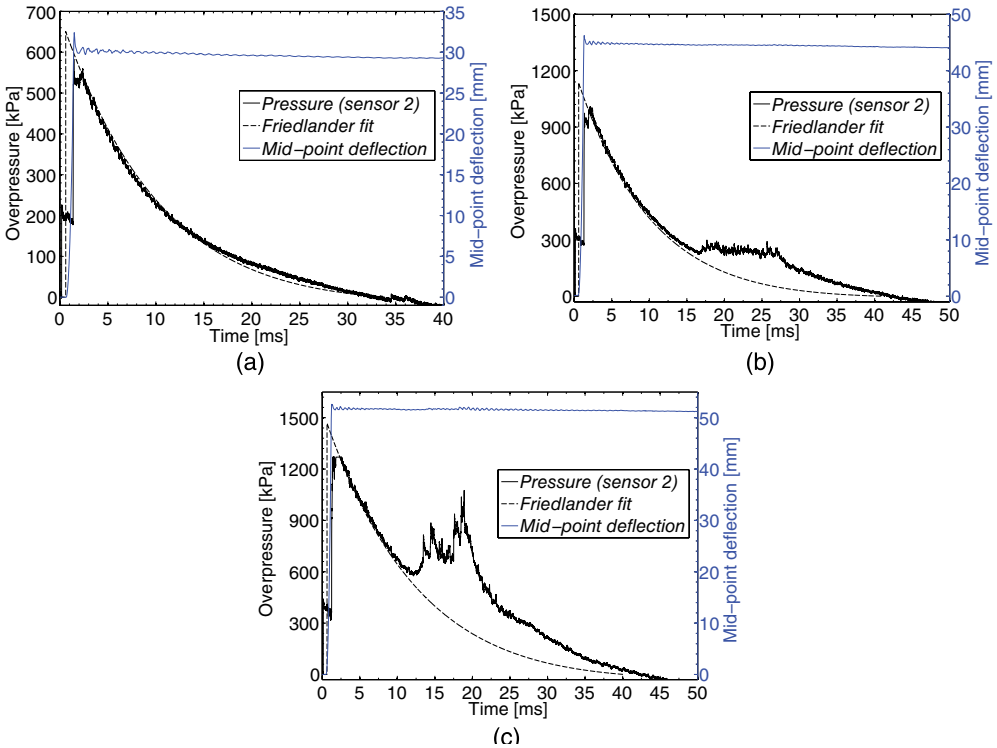

Figure 9. Synchronized pressure measurements (Sensor 2) and mid-point deflection during the deformable plate tests. The dashed line indicates the loading on a massive plate by curve-fitting the Friedlander equation and extrapolating this curve back to the time of impact: (a) D77-15, (b) D77-35 and (c) D77-60.

reduced reflected overpressure may be due to the deformation of the plates. This is also observed in previous studies which indicated that the blast mitigation could be related to the induced velocity in the plate (see, for example, Subramaniam et al., 2009), while Hanssen et al. (2002) suggested that the reduced pressure was due to the deformed shape which resembles a global dome. Since the permanent configuration is reached after approximately 1–2 ms (Figure 9) and that the FSI effect persists throughout the positive overpressure phase in Figure 10, this indicates that the reduction in the reflected overpressure may be a combination of both the movement and shape of the boundary. This is interesting in view of FSI and blast mitigation. It is, however, challenging to further identify which factor is more important for the observed decrease in pressure based on these experimental results. This therefore requires further investigations which will be performed in a subsequent study. Also note the good repeatability between tests with the same initial conditions by comparing the Mach number M_s for the corresponding tests in Tables 2 and 4.

Figure 11 shows selected 3D topography maps, contours of the transverse displacement field and deformation profiles at characteristic times during test D77-35, while displacement, strain and strain rate histories from selected elements in the 3D-DIC analysis are shown in Figure 12. The deformation is in accordance with the theory presented by Jones (2012) where plastic hinges start at the boundary corners (Figure 11(a)) and propagate along the diagonals towards the centre (Figure 11(b)) before they meet in the centre (Figure 11(c)), forming a square pyramidal with plastic hinges at the boundaries and along the diagonals of the plate. Based on these deformation fields, it is possible to

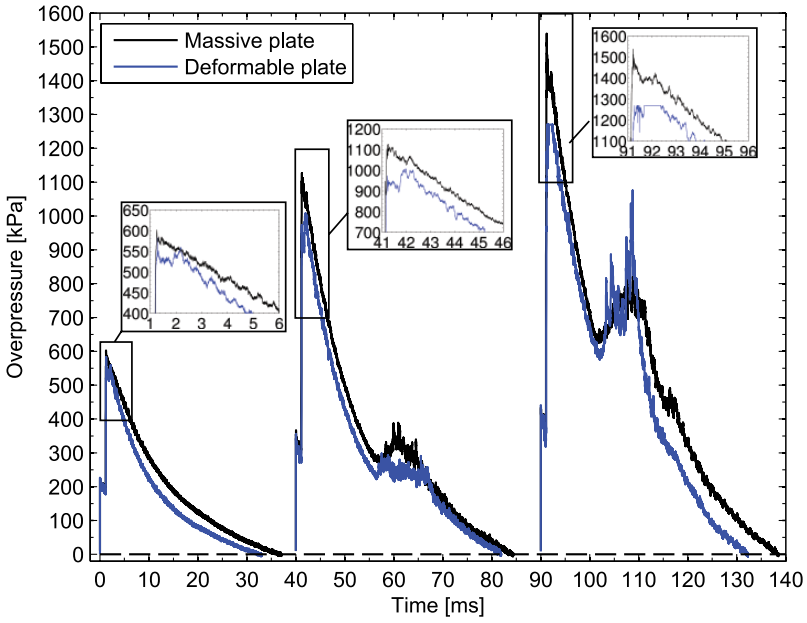

Figure 10. Investigation of FSI effects by comparing pressure measurements at Sensor 2 for experiments with massive and deformable plate with the same driver length and similar firing pressures. The pressure measurements are shifted in time to avoid confusions with each other.

Table 4. FSI effects observed by comparing the pressure measurements in the massive $p_{r,max}$ and deformable plate $p^{FSI}_{r,max}$ tests.

Test	Sensors 1–2	Experiments (Sensor 2)		
	M_s (−)	$p_{r,max}$ (kPa)	$p^{FSI}_{r,max}$ (kPa)	$\Delta p_{r,max}$ (%)
D77-15	1.63	591.6	555.6	−6.1
D77-35	1.88	1104.0	954.1	−13.6
D77-60	2.04	1487.6	1263.7	−15.1

Note that $p_{r,max}$, $p^{FSI}_{r,max}$ and $\Delta p_{r,max}$ refer to the measurements at Sensor 2 (Figure 2(a)) and not the peak pressure immediately after reflection from the plate.

obtain deformation histories (Figure 12(b)), strain histories (Figure 12(c)) and an indication of the corresponding strain rate histories (Figure 12(d)) in selected elements during the experiment. The selection of elements is shown in Figure 12(a). This is important information for the validation of computational methods in predicting the structural response during blast events. The 3D-DIC measurements may also be used to determine the dynamic material properties at intermediate strain rates $(10^1\,s^{-1} < \dot{\varepsilon} < 10^3\,s^{-1})$ and under biaxial response (Justusson et al., 2013). That is, the dynamic material properties can be obtained using the FE method and inverse modelling targeted against the experimental data. The use of the shock tube in such an approach is interesting because the deformable plates experience a non-uniform spatial and temporal strain rate distribution during the response from 0 to maximum deformation (Figure 12(d)). A single experiment could therefore be used to identify the dynamic material properties in the actual range of strain rates.

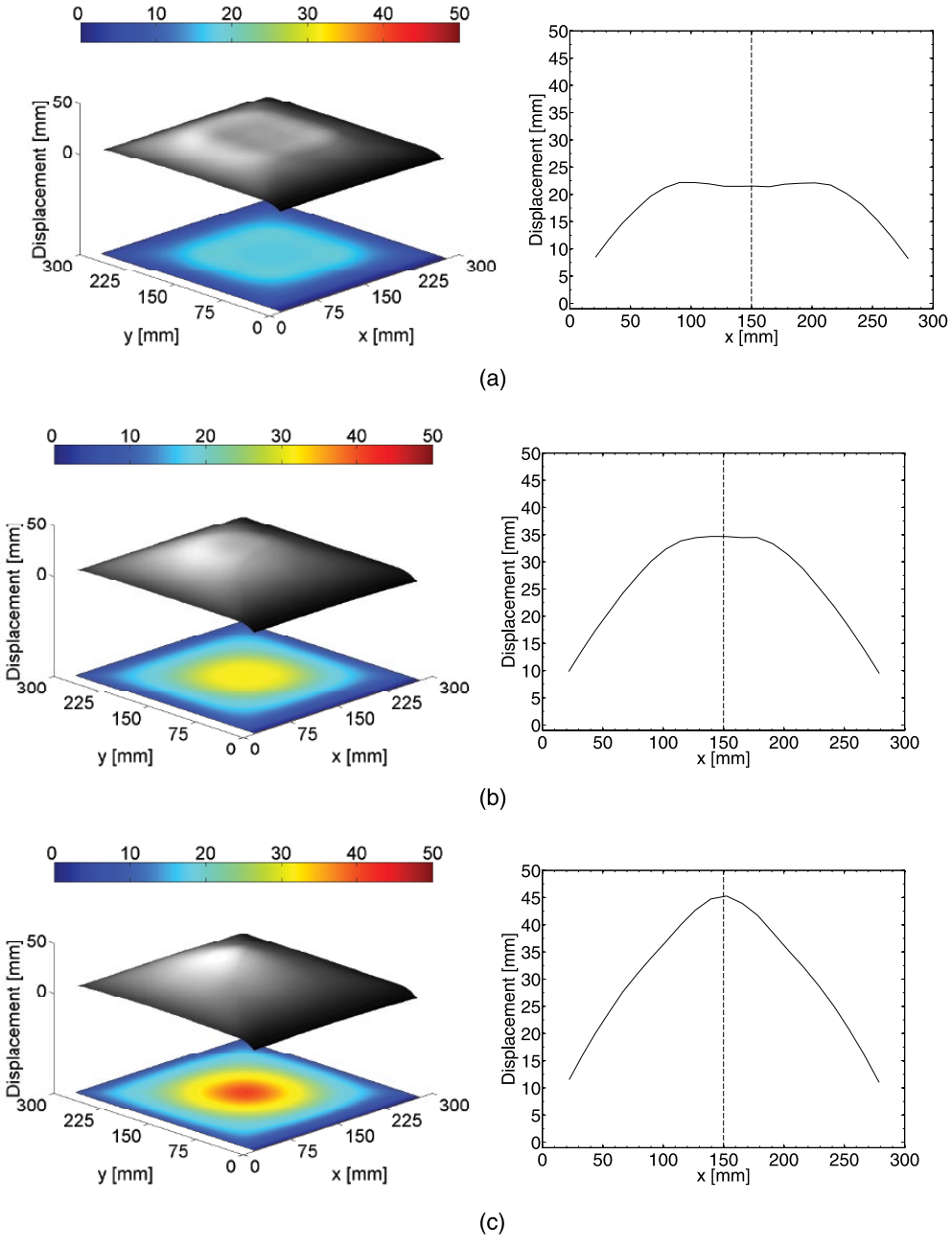

Figure 11. 3D topography maps and contours of the displacement field (left) and deformation profiles (right) at characteristic times in test D77-35: (a) $t = 1.084$ ms, (b) $t = 1.208$ ms and (c) $t = 1.334$ ms.

Note that all deformation profiles were corrected for the slight movement of the entire facility, and that the noise in the strain at the centre of the plate (Element 1 in Figure 12(c)) is due to the eigen oscillations of the laser mounting frame (Figure 2(e)) which caused the laser point to move

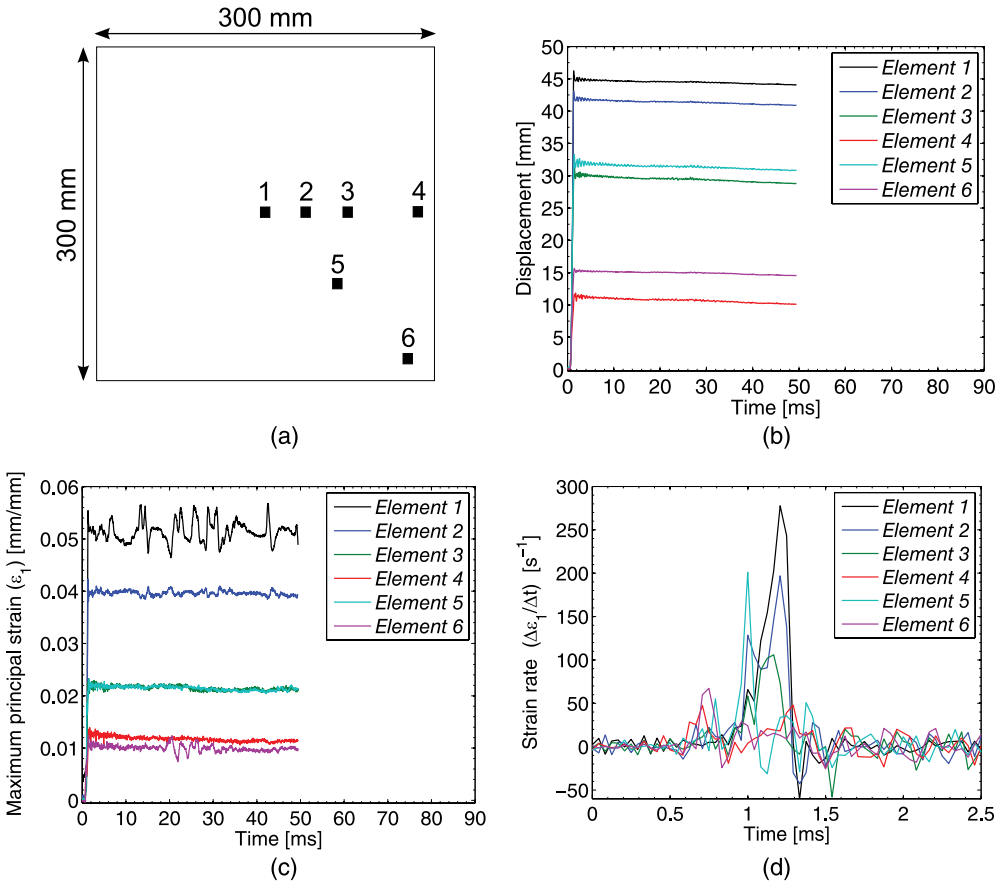

Figure 12. Displacement, strain and strain rate from selected elements in the 3D-DIC analysis of test D77-35: (a) selected elements, (b) displacement, (c) major principal strain and (d) strain rate.

and altered the greyscale value in this element. Still, this disturbance of the 3D-DIC occurs after the maximum deformation ($t = 1.334$ ms) and is not expected to effect the strain rate measurements during the time of interest (Figure 12(d)).

Numerical simulations

The numerical simulations were performed to evaluate the capabilities of the current computational methods in predicting the observations in the massive steel plate experiments and to investigate the wave patterns in more detail. All the numerical simulations were performed in the computer software EUROPLEXUS (2016), an explicit code jointly developed by the French Commissariat à l'énergie atomique et aux énergies alternatives (CEA DMT Saclay, France) and the Joint Research Centre (EC-JRC Ispra, Italy).

Since the SSTF is found to produce uniform shock waves over the cross section (Figure 4), these experiments are basically a one-dimensional (1D) problem. While an FE discretization is typical for structural applications, the most suitable discretization within computational fluid dynamics nowadays is based on finite volume (FV) formulations (Toro, 2009). FVs are another

way of expressing the conservation laws in which the governing equations for the computational cells are formulated and solved in integral form. This method is conservative since the formulation ensures that the flux entering a given volume is identical to that leaving the adjacent volume. Thus, the FV method requires less smoothness of the solution compared to the FE method, which is favourable in discontinuous solutions such as shock waves (Toro, 2009). The tube was therefore discretized as a 1D model using cell-centred finite volumes (*TUVF*) with a cell size of 10 mm. The diaphragm burst was assumed to be instantaneous and the firing section was not explicitly included in the numerical model. This implied that the initial discontinuity between the driver and driven sections was located at the beginning of the driven section at time $t = 0$. The cell size was determined based on a sensitivity study which showed that this mesh size is sufficient to capture the near-instantaneous rise in pressure and distinct peak reflected pressure. Due to the discrete nature (i.e. spatial discretization) of the data sampling in the numerical solution, discontinuities are represented by a finite slope since the pressure values are only defined at the centre of each computational cell. The variations can therefore not occur in less than one cell size. Stability in the convection phase of the explicit solution in time was ensured using a Courant–Friedrichs–Lewy (C_{CFL}) coefficient of 0.75. This was to ensure that the exchange of flux only occurred between neighbouring cells, that is, the fluid material could not be transported through more than one computational cell during one time step $\Delta t < C_{\mathrm{CFL}} \Delta L_{\mathrm{cell}} / a_{\max}$ where ΔL_{cell} is the length of the cell and $a_{\max}$ is the maximum wave speed at the current time step. The air was modelled using a perfect gas material (*GAZP*), and the initial conditions for each simulation were taken from the massive plate experiments in Table 1. The solution was obtained using an Eulerian formulation assuming a regular and fixed mesh with rigid boundary conditions at the fluid envelope and using the approximate HLLC Riemann solver proposed by Toro (2009) to calculate the numerical fluxes. It is noted that *TUVF* in EUROPLEXUS (2016) operates with a second-order accuracy in time and first-order accuracy in space for the HLLC solver. In this approach, the computational domain is basically considered as many neighbouring shock tubes to estimate the fastest signal velocity emerging from the initial discontinuity at the interface between the adjacent computational cells. The numerical solution assumed an inviscid flow using the Euler equations and will therefore serve as an idealized solution with zero energy loss.

Figure 5 compares the blast properties in the experiments and numerical simulations, while Figure 6 shows a comparison of the pressure–time histories for the representative tests discussed earlier. The blast properties from the numerical simulations in Figure 5 were extracted and calculated following the same procedure as in the experiments. In most of the cases, there is a good agreement between the numerical and experimental results. However, there seems to be a trend of increasing deviations at peak reflected overpressures $p_{\mathrm{r,max}}$ larger than 800 kPa (i.e. in test R27-60, R27-75, and R77-25 to R77-75). Figure 6 also confirms this trend. That is, the pressure histories are in good agreement in terms of the timing and magnitude of the incident pressures (Figure 6(a) to (f)), while the peak reflected pressures start to deviate from the numerical simulations at approximately 800 kPa (Figures 5(a) and 6(d) to (f)). Although the curves are shifted in time such that the time is equal to 0 when the shock wave arrives at Sensor 1, the timing of the direct jump from atmospheric pressure to peak reflected pressure at Sensor 3 and the recordings of the incident and reflected waves at Sensors 1 and 2 correspond well with the experimental measurements. This indicates that the simplified numerical model captures most of the events occurring in the experiments. However, there are also some physical phenomena that may not be predicted by this model. Possible explanations for these deviations may be a minor leakage of the pressure in the vicinity of the massive steel plate, the assumption of an instantaneous release of the high pressures in the simulations or a combination of both these events. In reality, there is some energy lost due to an initial 3D flow in the vicinity of the firing section during the diaphragm opening process (Andreotti et al., 2015).

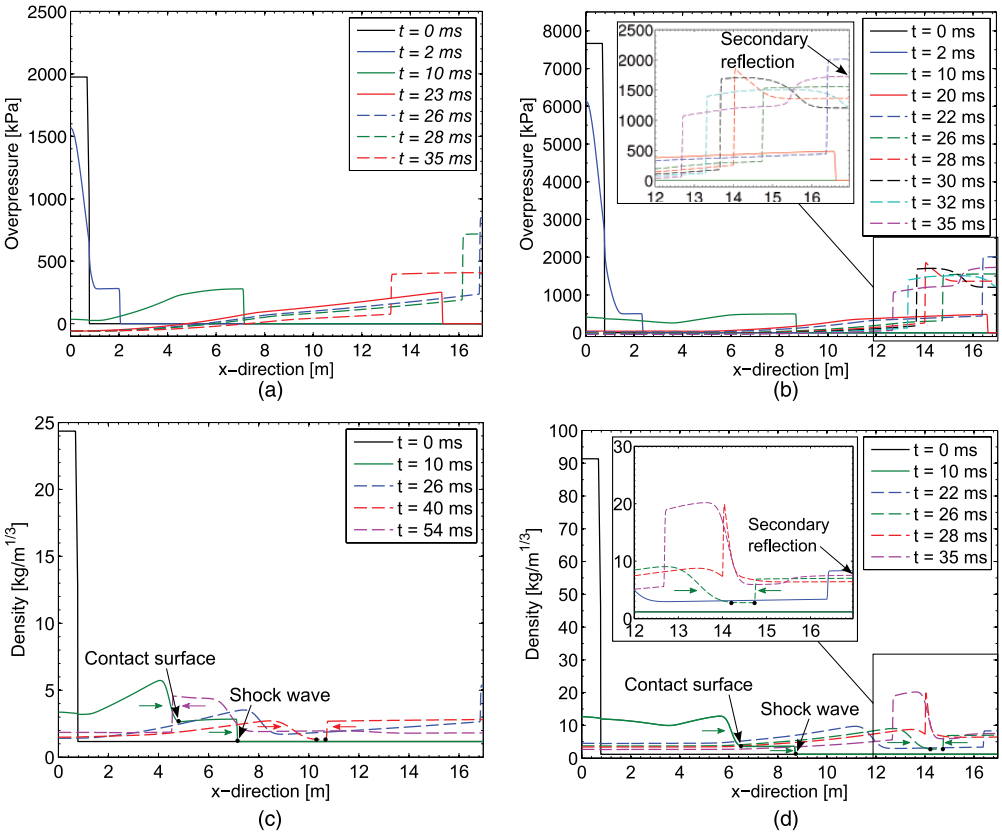

Figure 13. Pressure and density distribution along the longitudinal axis of the tube illustrating the wave pattern for representative tests: (a) pressure (R77-20), (b) pressure (R77-75), (c) density (R77-20) and (d) density (R77-75).

It is also seen that the numerical simulations predict the secondary and tertiary reflections observed in the experiments (Figure 6(e) and (f)). However, the tertiary reflections occur earlier in the simulations. A plausible explanation for this observation may be that the solenoid valves in the firing section remain open during the experiment. This allows for loss of directional energy (and velocity) when the waves reflect at the rear end of the driver section. Note that the tertiary reflection in tests R77-60 and R77-75 was observed before the reflected pressure returned to ambient conditions in the numerical simulations (Figure 6(f)). This implies that the corresponding values in Figure 5(c) are somewhat underestimated, since the end of the positive phase duration in these simulations was taken as the point of the tertiary reflection. Figure 13 contains the pressure and density profiles along the longitudinal axis of the tube at characteristic times for representative tests. R77-20 (Figure 13(a)) follows (to a large extent) the schematic representation given in section 'Shock tube principle and operation for blast applications', while R77-75 (Figure 13(b)) shows that the relative strength between the left-running reflected shock wave and the remaining right-running flow (contact surface and rarefaction waves illustrated as region *E* in Figure 1(e)) produces a secondary reflection at the right end of the tube after 35 ms to obtain pressure equilibrium. This is the same secondary reflection as that seen in Figure 6(f), where it should be noted that the time

is corrected for the time of arrival ($t_a \approx 21$ms) at Sensor 1 in Figure 6(f). The secondary reflections occur before the reflected shock wave interacts with the end of the driver section (left end of Figure 13). This may be explained by studying the density profiles along the tube because the contact surface represents the mass motion of the gas compressed by the shock wave and therefore also a jump in density. Figure 13(c) and (d) shows that the secondary reflection depends on the momentum and timing of the impact between the contact surface and the reflected shock wave. Although the remaining tail of the right-running wave has smaller magnitudes in the pressure compared to the reflected left-running shock front (Figure 13(a) and (b)), the velocity of the reflected shock is decreasing as it travels through the remaining tail of the right-running wave. Moreover, depending on the relative strength in the density at the interface between the (right-running) contact surface and the (left-running) reflected wave, there may be an increase in the density behind the reflected wave to restore pressure equilibrium (Figure 13(d)). This is seen as a second peak on the pressure measurements at the massive plate in Figure 6(e) and (f) during the exponential decay to ambient conditions and illustrates the importance of choosing a suitable combination of driver length and driver pressure to produce pressure profiles similar to that in idealized blast environments.

Conclusions

The shock tube presented in this study is found to produce a positive phase loading similar to that of an unconfined far-field airblast, and the recorded incident Mach numbers showed that the pressure measurements are in good agreement with the idealized shock tube theory. Several pressure transducers were positioned upstream and on a massive steel plate located at the tube end to measure the incident and reflected overpressures. The spatial and temporal distribution was found to be planar over the cross section, and the positive phase of the blast loading was obtained using a relatively long driven section. Moreover, the blast parameters were found to be a function of driver length and driver pressure.

An in-house 3D-DIC technique was evaluated by clamping thin steel plates at the tube end. Synchronization of the 3D-DIC and pressure measurements enabled a thorough investigation of the entire experiment and identification of possible FSI effects. These effects were investigated by comparing the loading on massive and deformable plates with similar initial conditions. A trend of reduced reflected pressures was found by allowing for finite deformations and inelastic strains in the plate. Finally, simplified 1D numerical simulations of the wave patterns were found to be in reasonable agreement with the experimental observations.

The main conclusion of this study is that the presented shock tube facility has proven to be a reliable alternative to explosive detonations and can be used to study the dynamic response and FSI of blast-loaded structures. Such investigations are important for experimental validation in the development and evaluation of advanced computational methods often required in blast-resistant design.

Acknowledgements

Dr Folco Casadei is gratefully acknowledged for his support and helpful comments during the preparation of the numerical model in EUROPLEXUS. The authors would also like to express their gratitude to Mr Trond Auestad and Mr Tore Wisth from CRI-CASA for their contributions during the experimental work.

Declaration of conflicting interests

The author(s) declared no potential conflicts of interest with respect to the research, authorship and/or publication of this article.

Funding

The author(s) received no financial support for the research, authorship and/or publication of this article.

References

Andreotti R, Colombo M, Guardone A, et al. (2015) Performance of a shock tube facility for impact response of structures. *International Journal of Non-Linear Mechanics* 72: 53–66.

Aune V, Børvik T and Langseth M (2015) Behaviour of plated structures subjected to blast loading. *EPJ Web of Conferences* 94: 01015.

Aune V, Fagerholt E, Hauge KO, et al. (2016) Experimental study on the response of thin aluminium and steel plates subjected to airblast loading. *International Journal of Impact Engineering* 90: 106–121.

Baker WE, Westine PS and Dodge FT (1991) *Similarity Methods in Engineering Dynamics: Theory and Practice of Scale Modeling* (Revised Edition). Amsterdam: Elsevier Science Publishers B.V.

Besnard G, Hild F and Roux S (2006) 'Finite-element' displacement fields analysis from digital images: application to Portevin-Le Chatelier effect. *Experimental Mechanics* 46: 789–804.

Børvik T, Hanssen AG, Langseth M, et al. (2009) Response of structures to planar blast loads – a finite element engineering approach. *Computers & Structures* 87: 507–520.

Chennamsetty ARK, LeBlanc J, Abotula S, et al. (2015) Dynamic response of Hastelloy® X plates under oblique shocks: experimental and numerical studies. *International Journal of Impact Engineering* 85: 97–109.

Colombo M, Di Prisco M and Martinelli P (2011) A new shock tube facility for tunnel safety. *Experimental Mechanics* 51(7): 1143–1154.

Courant R and Friedrichs KO (1976) *Supersonic Flow and Shock Waves*. New York: Springer-Verlag.

Downes S, Knott A and Robinson I (2014) Towards a shock tube method for the dynamic calibration of pressure sensors. *Philosophical Transactions of the Royal Society A: Mathematical, Physical and Engineering Sciences* 372(2023): 299–316.

EUROPLEXUS (2016) *User's Manual*. Available at: http://europlexus.jrc.ec.europa.eu/public/manual_pdf/manual.pdf (accessed 5 August 2016).

Fagerholt E (2012) *Field measurements in mechanical testing using close-range photogrammetry and digital image analysis*. PhD Thesis, Norwegian University of Science and Technology (NTNU), Trondheim.

FEMA 452 (2005) *Risk Assessment: Mitigate Potential Terrorist Attack against Buildings*. Washington DC: US Department of Homeland Security.

Friedlander FG (1946) The diffraction of sound pulses. I. Diffraction by a semi-infinite plane. *Proceedings of the Royal Society A: Mathematical, Physical and Engineering Sciences* 186(1006): 322–344.

Gaydon AG and Hurle IR (1963) *The Shock Tube in High-Temperature Chemical Physics*. London: Chapman & Hall Ltd.

Hanssen AG, Enstock L and Langseth M (2002) Close-range blast loading of aluminium foam panels. *International Journal of Impact Engineering* 27: 593–618.

Harris C and Stevens M (1988) A combined corner and edge detector. In: *Proceedings of the 4th Alvey vision conference*, Manchester, pp. 189–192. Available at: http://www.bmva.org/bmvc/1988/avc-88-000.pdf

Heikkilä J (1997) *Accurate camera calibration and feature based 3-D reconstruction from monocular image sequences*. PhD Thesis, University of Oulo, Oulo.

Hild F, Raka B, Baudequin M, et al. (2002) Multiscale displacement field measurements of compressed mineral wool samples by digital image correlation. *Applied Optics* 41: 6815–6828.

ISO 16934 (2007) Glass in building – explosion-resistant security glazing – test and classification by shock-tube loading.

Jones N (2012) *Structural Impact* (2nd edn). Cambridge: Cambridge University Press.

Justusson B, Pankow M, Heinrich C, et al. (2013) Use of a shock tube to determine the bi-axial yield of an aluminium alloy under high rates. *International Journal of Impact Engineering* 58: 55–65.

Kambouchev N, Noels L and Radovitzky R (2007) Numerical simulation of fluid-structure interaction between air blast waves and free-standing plates. *Computers & Structures* 85(11–14): 923–931.

Kingery CN and Bulmash G (1984) *Airblast Parameters from TNT Spherical Air Burst and Hemispherical Surface Burst*. Aberdeen Proving Ground, MD: Defence Technical Information Center, Ballistic Research Laboratory.

Langdon GS, Rossiter IB, Balden VH, et al. (2010) Performance of mild steel perforated plates as blast wave mitigation technique: experimental and numerical investigation. *International Journal of Impact Engineering* 37: 1021–1036.

Larcher M and Casadei F (2010) Explosions in complex geometries – a comparison of several approaches. *International Journal of Protective Structures* 1(2): 169–195.

LeBlanc J, Shukla A, Rousseau C, et al. (2007) Shock loading of three-dimensional woven composite materials. *Composite Structures* 79: 344–355.

Little RG (2007) Cost-effective strategies to address urban terrorism: a risk management approach. In: Richardson HW, Gordon P and Moore JE II (eds) *The Economic Costs and Consequences of Terrorism*. Edward Elgar Publishing Ltd, pp. 98–115.

Lloyd A, Jacques E, Saatcioglu M, et al. (2010) Capabilities of a shock tube to simulate blast loading on structures. *American Concrete Institute (ACI) Special Publication* 281: 35–54.

Louar MA, Belkassem B, Ousji H, et al. (2015) Explosive driven shock tube loading of aluminium plates: experimental study. *International Journal of Impact Engineering* 86: 111–123.

NS-EN 13123-1 (2001) Windows, doors and shutters – explosion resistance – requirements and classification – part 1: shock tube.

NS-EN 13124-1 (2001) Windows, doors and shutters – rest method – part 1: shock tube.

NS-EN 13445 (2014) Unfired pressure vessels.

Riedel W, Mayrhofer C, Thoma K, et al. (2010) Engineering and numerical tools for explosion protection of reinforced concrete. *International Journal of Protective Structures* 1(1): 85–101.

Rigby SE, Tyas A, Clarke SD, et al. (2015) Observations from preliminary experiments on spatial and temporal pressure measurements from near-field free air explosions. *International Journal of Protective Structures* 6(2): 175–190.

Sturm P and Maybank S (1999) On plane-based camera calibration: a general algorithm, singularities, applications. In: *Proceedings of the IEEE conference on computer vision and pattern recognition*, Fort Collins, CO, 23–25 June, pp. 432–437. New York: IEEE.

Subramaniam KV, Nian W and Andreopoulos Y (2009) Blast response simulation of an elastic structure: evaluation of the fluid-structure interaction effect. *International Journal of Impact Engineering* 36: 965–974.

Sutton MA, Orteu J-J and Schreier HW (2009) *Image Correlation for Shape, Motion and Deformation Measurements – Basic Concepts, Theory and Applications*. New York: Springer Science & Business Media.

Toro EF (2009) *Riemann Solvers and Numerical Methods for Fluid Dynamics – A Practical Introduction* (3rd edn). Berlin, Heidelberg: Springer-Verlag.

UFC 3-340-02 (2008) *Structures to Resist the Effects of Accidental Explosions*. Washington, DC: US Department of Defence.

Vaziri A and Hutchinson JW (2007) Metal sandwich plates subjected to intense air shocks. *International Journal of Solids and Structures* 44: 2021–2035.